nature communications

Article

https://doi.org/10.1038/s41467-025-63722-6

Interface engineering of single-molecular heterojunction catalysts for CO_2 electroreduction in strong acid medium

Received: 1 April 2025

Accepted: 28 August 2025

Shanhe Gong[1,2,3,4,8], **Yanjie Zhai**[2,8], **Chengkai Jin**[5,8], **Han Xu**[3], **Qing Xia**[2], **Weisong Li**[2], **Yiran Ying**[6], **Jie Wu**[2], **Xiaojie She**[1], **Zhaolong Wang**[1], **Xiaomeng Lv**[3] ✉, **Chundu Wu**[4], **Kangcheung Chan**[7], **Xunhua Zhao**[5] ✉, **Xiao Zhang**[2] ✉ & **Shu Ping Lau**[1] ✉

Electrochemical carbon dioxide reduction reaction (CO_2RR) under strongly acidic conditions enables high CO_2 utilization. However, especially in proton exchange membrane (PEM) electrode assembly reactors, achieving selective CO_2RR in such environments remains challenging due to uncontrolled interfacial water diffusion at high current densities. Here, we develop a nickel-based heterogeneous molecular electrocatalyst (NiPc-NH_2/CNT-SHP) featuring amino (-NH_2) functional groups and grafted long-chain hydrophobic molecules. Under acidic conditions, -NH_2 is in situ protonated to form amino cations (-NH_3^+). The positively charged -NH_3^+ groups and hydrophobic molecules effectively disrupt the protonated water (H_3O^+)-rich network, inhibiting the invasion of H_3O^+ and thereby suppressing the hydrogen evolution reaction, while enhancing selectivity for acidic CO_2RR. The catalyst achieves nearly 100% Faradaic efficiency for CO at current densities from 50 to 400 mA cm^{-2}, with approximately 76% CO_2 utilization efficiency in a flow cell, and sustains over 80% selectivity for more than 200 h in a self-designed PEM–porous solid electrolyte reactor. These findings highlight interfacial water management as a key design principle for efficient acidic CO_2 electroreduction.

Converting CO_2 into high-value-added chemicals and fuels through the electrocatalytic carbon dioxide reduction reaction (CO_2RR) is a promising approach for producing valuable fuels and addressing carbon emissions[1,2]. CO_2RR systems predominantly employ alkaline or neutral electrolytes due to the interfacial alkaline environment, which can promote the conversion of CO_2 molecules into *COOH (adsorbed carboxyl intermediate) and suppress the competing hydrogen evolution reaction (HER)[3–5]. However, the alkaline solution exhibits a low CO_2 utilization efficiency, with theoretically 75% of the input CO_2 reacting with hydroxide (OH^-) to form carbonate (CO_3^{2-}), which then enters the anode through the anion exchange membrane (AEM), resulting in CO_2 loss[5–8]. Additionally, the continuous influx of CO_2

---

[1]Department of Applied Physics, Research Institute for Smart Energy, The Hong Kong Polytechnic University, Hung Hom, Kowloon, Hong Kong SAR, China. [2]Department of Mechanical Engineering, The Hong Kong Polytechnic University, Hung Hom, Kowloon, Hong Kong SAR, China. [3]School of Chemistry and Chemical Engineering, Jiangsu University, Zhenjiang, P. R. China. [4]School of Agricultural Engineering, Jiangsu University, Zhenjiang, P. R. China. [5]Key Laboratory of Quantum Materials and Devices of Ministry of Education School of Physics, Southeast University, Nanjing, P. R. China. [6]State Key Laboratory of Solidification Processing, Center for Nano Energy Materials, Northwestern Polytechnical University and Shaanxi Joint Laboratory of Graphene (NPU), Xi'an, P. R. China. [7]Department of Industrial and Systems Engineering and Research Institute for Advanced Manufacturing, The Hong Kong Polytechnic University, Hung Hom, Kowloon, Hong Kong SAR, China. [8]These authors contributed equally: Shanhe Gong, Yanjie Zhai, Chengkai Jin. ✉e-mail: lvxm@ujs.edu.cn; xhzhao@seu.edu.cn; xiao1.zhang@polyu.edu.hk; apsplau@polyu.edu.hk

lowers the electrolyte pH, disrupting the catalyst interface microenvironment and compromising both membrane integrity and catalyst stability[9].

In response to this dilemma, increasing attention has shifted toward electrocatalytic CO_2 reduction in acidic media, which offers significant advantages for efficient CO_2 conversion. In acidic systems (pH <4), CO_3^{2-} or HCO_3^- (bicarbonate) formed at the electrode interface can rapidly reconvert to CO_2 upon diffusing into the bulk electrolyte, thereby minimizing the loss of CO_2 and reduction products[9–13]. However, the high-concentration acidic environment poses significant challenges to catalysts and the efficiency of electrocatalytic CO_2 reduction, especially in acidic PEM reactors. Most metal catalysts and metal oxides are primarily susceptible to corrosion in acidic solutions, leading to catalyst deactivation[13–16]. Additionally, the high concentration of protons (H^+) intensifies HER competition[11,17,18], resulting in poor Faradaic efficiency (FE) of CO_2RR at high current densities. Therefore, strategies that enhance CO_2RR activity while suppressing HER remain critical for practical applications.

Recently, numerous studies have demonstrated that alkali metal cations are attracted to the negatively charged cathode field, resulting in their accumulation in the cathode capacitor layer and the formation of cation shielding. The formed OH^- though HER or CO_2RR will be preserved by cation shielding. Therefore, the local cathode environments, initially rich in a protonated water (H_3O^+) network, can be transformed into an alkaline environment[19,20], effectively mitigating the competing HER in an acidic medium and thus improving the poor Faradaic efficiency of CO_2RR[21–23]. Additionally, CO_3^{2-} or HCO_3^- species formed at the cathode surface diffuse into the electrolyte, where they react with acid to produce CO_2 molecules that subsequently return to the catalyst interface, maintaining a high carbon utilization efficiency. However, due to the strong Coulomb attraction to H_3O^+ at more negative potentials[24], the catalyst interface makes it challenging to resist the invasion of harmful water species. A significant amount of H_3O^+ is rapidly introduced into the electric double layer, which disrupts the alkaline environment of the double layer on the cathodic catalyst, thereby facilitating HER. Therefore, the high FE of acidic CO_2RR is limited to a small current window, as HER increasingly dominates at high current densities, limiting practical applications.

Herein, we develop a superhydrophobic heterogeneous molecular catalyst ($NiPc\text{-}NH_2/CNT\text{-}SHP$) featuring amino ($-NH_2$) functional groups and long-chain hydrophobic molecules (octadecylamine) grafted on multi-walled carbon nanotubes (CNT). Under acidic conditions, $-NH_2$ undergoes in-situ protonation to form amino cations ($-NH_3^+$), which could repel H_3O^+ via Coulombic repulsion, effectively suppressing HER activity. Simultaneously, the long-chain hydrophobic molecules modulate the interfacial water network, optimizing the ratio of free water to hinder H_2O reduction and facilitate CO_2RR under strongly acidic conditions (pH = 1). Therefore, the $NiPc\text{-}NH_2/CNT\text{-}SHP$ achieves a high CO Faraday efficiency (FE_{CO}) of nearly 100% across a broad current density window of 50 to 400 mA cm^{-2}, with a carbon monoxide (CO) partial current density of 426 ± 14 mA cm^{-2}, and high single-pass CO_2 conversion efficiency in the flow cell. Thanks to the stable hydrophobic and amino groups, a proton-exchange membrane (PEM)-based porous solid electrolyte (PEM-PSE) reactor was developed to enable continuous, selective (> 80%), and stable (> 200 h) CO production using $NiPc\text{-}NH_2/CNT\text{-}SHP$ as the cathode for practical applications.

Results

Catalyst design and preparation

To achieve high selective CO_2RR in the PEM reactor, the first step is to strategically design the catalytic site to suppress the competitive reaction of HER under high currents. We select a Ni-based molecular catalyst due to its well-defined $Ni–N_4$ coordination center, which imposes a high energy barrier for HER[25,26]. Additionally, to mitigate H_3O^+ intrusion at the catalyst interface, we aim to establish a built-in positive electric field that repels H_3O^+ via Coulombic repulsion. Given that the protonation of amino ($-NH_2$) groups into amino cations ($-NH_3^+$) under acidic conditions is a thermodynamically spontaneous process, we are inspired to employ amino-functionalized Ni phthalocyanine ($NiPc\text{-}NH_2$) as the catalytic unit. Under acidic conditions, $-NH_2$ spontaneously converts into $-NH_3^+$, which is expected to effectively slow down the invasion of H_3O^+ into the catalyst's surface during acidic CO_2RR.

However, introducing a positively charged interface inherently increases affinity for H_2O (excluding H_3O^+)[27], thereby promoting undesired H_2O reduction. To counteract this effect, we further engineer a hydrophobic interface by incorporating octadecylamine as a long-chain hydrophobic modifier, which modulates the interfacial water network and reduces H_2O reduction activity. Integrating these design strategies, (1) Coulombic repulsion via interfacial charge modulation and (2) hydrophobic surface engineering, are expected to achieve highly selective acidic CO_2RR at high current in the PEM reactor.

Synthesis and characterization of the $NiPc\text{-}NH_2/CNT\text{-}SHP$ catalyst

Following this design strategy, we synthesized the superhydrophobic $NiPc\text{-}NH_2/CNT\text{-}SHP$ catalyst. First, $NiPc\text{-}NH_2$, the molecular catalytic unit, was synthesized by hydrothermal and Soxhlet extraction (see Supplementary Methods, Supplementary Figs. S1, 2)[28,29]). Commercial carboxyl-modified carbon nanotubes (CNT-COOH) were converted to acyl chloride-functionalized CNTs (CNT-COCl) through an acyl chlorination reaction under anhydrous and inert conditions. Subsequently, $NiPc\text{-}NH_2$ and octadecylamine were grafted onto CNT-COCl via nucleophilic substitution, forming the $NiPc\text{-}NH_2/CNT\text{-}SHP$ catalyst (Supplementary Fig. S3, and Fig. 1a). For comparison, catalysts without hydrophobic modification ($NiPc\text{-}NH_2/CNT$) and without amino functionalization (NiPc@CNT) were also synthesized (see Supplementary methods).

To characterize the structural and morphological features of $NiPc\text{-}NH_2/CNT\text{-}SHP$, we conducted X-ray diffraction (XRD, Supplementary Fig. S4), infrared spectroscopy (Supplementary Figs. S5, S6), and ultraviolet–visible spectroscopy (UV-Vis, Supplementary Fig. S7), confirming the successful grafting of unordered $NiPc\text{-}NH_2$ and octadecylamine onto CNT. Field-emission scanning electron microscopy (SEM, Supplementary Fig. S8) and transmission electron microscopy (TEM, Supplementary Fig. S7) images revealed that $NiPc\text{-}NH_2/CNT\text{-}SHP$ retains the characteristic one-dimensional morphology of CNT without the formation of aggregated $NiPc\text{-}NH_2$ crystals (Supplementary Fig. S9), indicating uniform Ni molecular site distribution. Aberration-corrected high-angle annular dark-field scanning transmission electron microscopy (AC HAADF-STEM) further showed the presence of atomically dispersed Ni sites, as evidenced by the bright spots observed in Fig. 1b (yellow). Meanwhile, the water contact angle measurements found that the hydrophobicity of the interface changed, $NiPc\text{-}NH_2/CNT\text{-}SHP$ exhibited a contact angle of ~151° (Fig. 1c), significantly higher than pristine CNT (~ 22°, Supplementary Fig. S9b) and $NiPc\text{-}NH_2/CNT$ (~ 109°, Supplementary Fig. S9c), confirming that octadecylamine has successfully introduced a superhydrophobic interface. Elemental mapping analysis further demonstrated the uniform distribution of Ni catalytic sites (Supplementary Fig. S10) across the CNT. Moreover, inductively coupled plasma mass spectrometry (ICP-MS) determined the Ni content in $NiPc\text{-}NH_2/CNT$ and $NiPc\text{-}NH_2/CNT\text{-}SHP$ as 0.75 wt% and 0.73 wt%, respectively.

We performed X-ray photoelectron spectroscopy (XPS) to further elucidate the chemical states of elements in $NiPc\text{-}NH_2/CNT\text{-}SHP$ (Fig. 1d, and Supplementary Figs. S11–13). Compared to $NiPc\text{-}NH_2$ (Fig. 1d) and NiPc/CNT (Supplementary Fig. S14), $NiPc\text{-}NH_2/CNT$ (Supplementary Fig. S12) and $NiPc\text{-}NH_2/CNT\text{-}SHP$ exhibited an

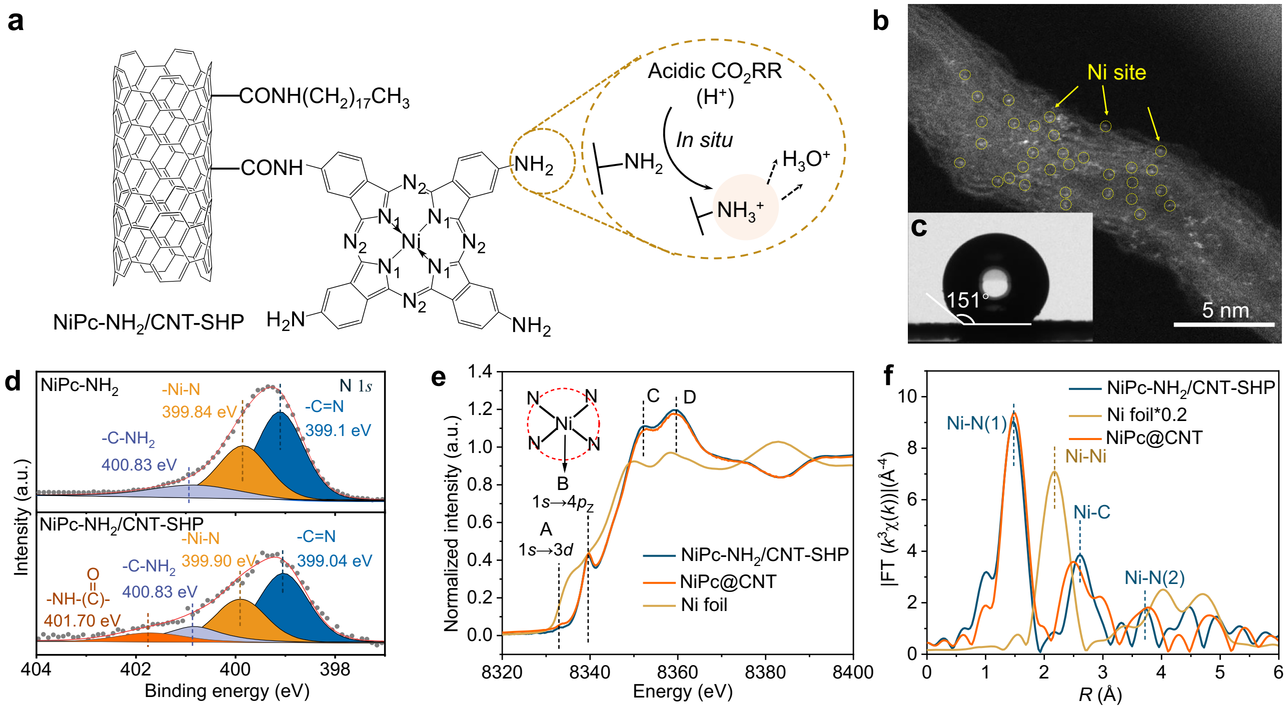

Fig. 1 | Synthesis and characterization of the NiPc-NH_2/CNT-SHP catalyst. **a** Mechanism diagram of the NiPc-NH_2/CNT-SHP catalyst. **b** AC HAADF-STEM image of NiPc-NH_2/CNT-SHP, with the inset showing (**c**) contact angles of water on NiPc-NH_2/CNT-SHP. **d** High-resolution XPS N 1*s* spectra of NiPc-NH_2, and NiPc-NH_2/CNT-SHP. **e** Experimental Ni K-edge XANES spectra and first derivative curves and (**f**) Fourier transformed magnitudes of the experimental Ni K-edge EXAFS signals of NiPc-NH_2/CNT-SHP, NiPc@CNT, and Ni foil. Source data are provided as a Source Data file.

additional peak at 401.70 eV, attributed to the –NH–(C = O)– species[30], confirming the successful grafting of both NiPc-NH_2 and hydrophobic functional groups onto CNT. The absence of shifts in Ni binding energy between NiPc-NH_2/CNT and NiPc-NH_2/CNT-SHP relative to NiPc-NH_2 (Supplementary Fig. S13) suggests that the central coordination structure remains intact after chemical grafting. To determine the geometric structure of the Ni sites in NiPc-NH_2/CNT-SHP, we conducted synchrotron X-ray absorption spectroscopy measurements (XAS). The X-ray absorption near-edge structure (XANES, Fig. 1e) revealed distinct spectral features, indicating differences in Ni coordination compared to the Ni foil and suggesting a higher Ni oxidation state. Furthermore, a weak pre-edge peak (peak A) and a pronounced 1*s* → 4*pz* transition (peak B) were observed, indicative of high D_{4h} centro-symmetry[31]. The extended X-ray absorption fine structure (EXAFS) Fourier transform (FT) spectrum of NiPc-NH_2/CNT-SHP displayed a primary peak at 1.47 Å (Fig. 1f), corresponding to Ni–N scattering in the first coordination shell, and well below the Ni–Ni bond distance (2.17 Å), illustrating that the absence of Ni clusters or nanoparticle aggregation. Figure 1e, f show that the XANES and EXAFS spectra of NiPc@CNT closely resemble those of NiPc-NH_2/CNT-SHP, indicating a similar local coordination environment around the Ni center. Furthermore, only a single intensity maximum at 5.9 $Å^{-1}$ was identified in NiPc-NH_2/CNT-SHP (Supplementary Fig. S15a), corresponding to Ni–N coordination. This characteristic, also observed in NiPc@CNT (6.2 $Å^{-1}$, Supplementary Fig. S15c), clearly distinguishes both samples from Ni foil (Supplementary Fig. S15b). These structural characterizations confirm the successful synthesis of NiPc-NH_2/CNT-SHP with hydrophobic groups and NiPc-NH_2 while preserving the well-defined Ni–N_4 structure sites, in line with our design strategy.

Electrochemical acidic CO_2RR performance in flow cell

Given that the structural characterization of the catalyst aligns with our initial design, we evaluated the electrochemical acid CO_2RR performance in the flow cell (Supplementary method). In a strong-acid environment (0.5 M $K_2SO_4 + H_2SO_4$ (pH = 1)), online gas chromatography analysis identified CO and hydrogen (H_2) as the only gas-phase products, while liquid-phase products were undetectable by ^{1}H Nuclear Magnetic Resonance (NMR) spectroscopy (Supplementary Fig. S17). The NiPc-NH_2/CNT-SHP, NiPc-NH_2/CNT, and NiPc@CNT catalysts exhibited current densities of 35 mA cm^{-2} at –1.04, –1.04, and –1.13 V versus the reversible hydrogen electrode (*vs.* RHE), respectively, with 80% *iR* compensation (Fig. 2a), consistent with recent reports[32]. Furthermore, NiPc-NH_2/CNT-SHP achieved a current density of 500 mA cm^{-2} at –1.60 V *vs.* RHE, which is lower than that of NiPc-NH_2/CNT (–1.81 V *vs.* RHE) and NiPc@CNT (–1.88 V *vs.* RHE), highlighting the structural advantages of NiPc-NH_2/CNT-SHP in optimizing catalytic activity.

We further analyzed the relationship between current and FE_{CO} (Fig. 2b). NiPc-NH_2/CNT-SHP exhibited high CO selectivity (FE_{CO} > 98%) over a wide current density range (50–400 mA cm^{-2}), maintaining a FE_{CO} of 85.26% at 500 mA cm^{-2}, outperforming both NiPc-NH_2/CNT and NiPc@CNT. Interestingly, the FE_{CO} of NiPc@CNT declined significantly beyond 250 mA cm^{-2}, reaching 49.50% at 300 mA cm^{-2} (Fig. 2b). However, when the test condition is alkaline (1 M KOH), NiPc@CNT maintained a high FE_{CO} of 95.84% at 350 mA cm^{-2} (Supplementary Fig. S18b), comparable to NiPc-NH_2/CNT, indicating that the in situ generated -NH_3^+ effectively mitigates interfacial acidity, thereby enhancing acidic CO_2RR selectivity at high current densities.

The introduction of interfacial hydrophobic molecules also optimizes the performance of Ni sites under acidic conditions (Fig. 2c and Supplementary Fig. S19). As seen in Fig. 2c, NiPc-NH_2/CNT-SHP exhibited a maximal j_{CO} of 426 mA cm^{-2} at –1.60 V *vs.* RHE (Fig. 2c), with the production rate of 7.97 mmol cm^{-2} h^{-1} (Fig. 2d), which is better than that of NiPc-NH_2/CNT (385 mA cm^{-2}, 6.78 mmol cm^{-2} h^{-1}), and NiPc@CNT (198 mA cm^{-2}, 4.61 mmol cm^{-2} h^{-1}). Furthermore, NiPc-NH_2/CNT-SHP demonstrated the highest CO turnover frequency (TOF_{CO}) is 17.76 s^{-1} (63936 h^{-1}, Fig. 2e) compared to NiPc-NH_2/CNT (14.70 s^{-1}) and

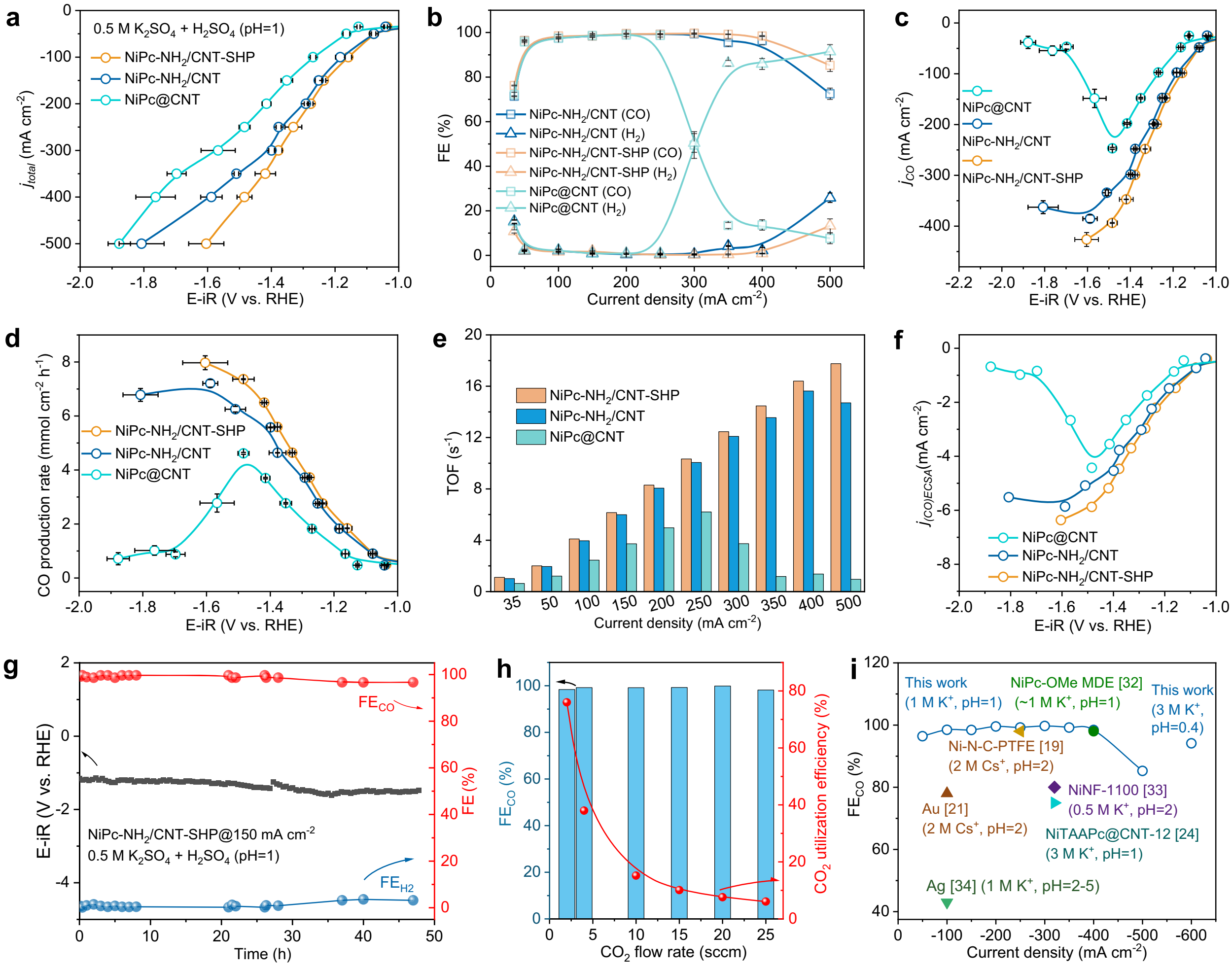

Fig. 2 | Electrochemical acidic CO_2RR performance in flow cell. a j_{total} (80% iR compensation), **b** FE_{CO}, **c** j_{CO} (80% iR compensation), **d** CO production rate (80% iR compensation), **e** TOF_{CO}, **f** $j_{(CO)ECSA}$ (80% iR compensation) of NiPc-NH_2/CNT-SHP, NiPc-NH_2/CNT and NiPc@CNT in 0.5 M K_2SO_4 + H_2SO_4 (pH = 1), Resistance: 4.2 ± 0.42 Ω. **g** Total current density and FE_{CO} of NiPc-NH_2/CNT-SHP in acidic CO_2RR test (80% iR compensation). **h** Acid CO_2RR utilization efficiency of NiPc-NH_2/CNT-SHP with different CO_2 flow rates. **i** Comparison of acidic CO_2RR performance of NiPc-NH_2/CNT-SHP in flow cell with other reported catalysts. The error bars represent the standard deviation of three independent measurements. Source data are provided as a Source Data file.

NiPc@CNT (6.20 s^{-1}). The double-layer capacitance (C_{dl}) of NiPc-NH_2/CNT-SHP (2.68 mF cm^{-2}) was comparable to NiPc-NH_2/CNT (2.63 mF cm^{-2}) and NiPc@CNT (2.23 mF cm^{-2}) (Supplementary Fig. S20), enabling the CO partial current densities of NiPc-NH_2/CNT-SHP normalized by the electrochemical active surface area (ECSA) also to be higher than NiPc-NH_2/CNT and NiPc@CNT (Fig. 2f). Despite the stronger acidic environment (pH = 0.4), NiPc-NH_2/CNT-SHP is still able to achieve the maximal j_{CO} of 561 mA cm^{-2} (Supplementary Fig. S21c), which is still higher to that of NiPc@CNT (234 mA cm^{-2}, Supplementary Fig. S22c). Notably, the absence of a superhydrophobic interface in NiPc-NH_2/CNT resulted in small liquid accumulations at the back of the electrode after prolonged operation (Supplementary Fig. S24), with the overflowing liquid exhibiting an alkaline pH (Supplementary Fig. S25), consistent with previous reports[9]. In addition, NiPc-NH_2/CNT-SHP also achieves the highest activity of CO_2RR in alkaline and neutral solution, showing the maximal j_{CO} of 390 mA cm^{-2} at −0.70 V *vs.* RHE (1 M KOH, Supplementary Figs. S18a–c) and 414 mA cm^{-2} at −1.13 V *vs.* RHE (1 M $KHCO_3$, Supplementary Figs. S18d–f), indicating the good activity of NiPc-NH_2/CNT-SHP.

Given the performance of NiPc-NH_2/CNT-SHP, we then focus on a long-term test under high current density. Due to the absence of hydrophobic functionalization, NiPc-NH_2/CNT exhibited poor stability, with continuous operation limited to less than 2 h at 100 mA cm^{-2} (Supplementary Figs. S26, 27), during which FE_{CO} rapidly declined after 2 h. By contrast, NiPc-NH_2/CNT-SHP maintained stable operation at 150 mA cm^{-2} for over 48 h, with a consistent potential of around−1.37 V *vs.* RHE and FE_{CO} exceeding 96% (Fig. 2g), along with good stability in neutral and alkaline conditions (Supplementary Figs. S28, S29).

Furthermore, NiPc-NH_2/CNT-SHP significantly improved CO_2 utilization efficiency at high current densities. At 200 mA cm^{-2}, FE_{CO} reached ~98.41% as the CO_2 flow rate decreased from 25 to 2 mL min^{-1}, achieving a high single-pass carbon efficiency (SPCE) of ~76% at a flow rate of 2 mL min^{-1} (Fig. 2h). This performance under acidic conditions is further summarized in Supplementary Table S2 and Fig. 2i, where NiPc-NH_2/CNT-SHP demonstrates competitive FE_{CO} compared to previous reports in acidic environment[19,21,24,32–34].

Intrinsic activity analysis for CO_2RR performance

In order to verify the spontaneous formation and stability of amino cations under acidic conditions during electrochemical CO_2 reduction, we performed in situ XPS measurements in an acidic electrolyte (CO_2-saturated 0.5 M K_2SO_4 + H_2SO_4 (pH = 1)). Initially, the as-prepared NiPc-NH_2/CNT-SHP electrode showed no signal attributable to protonated

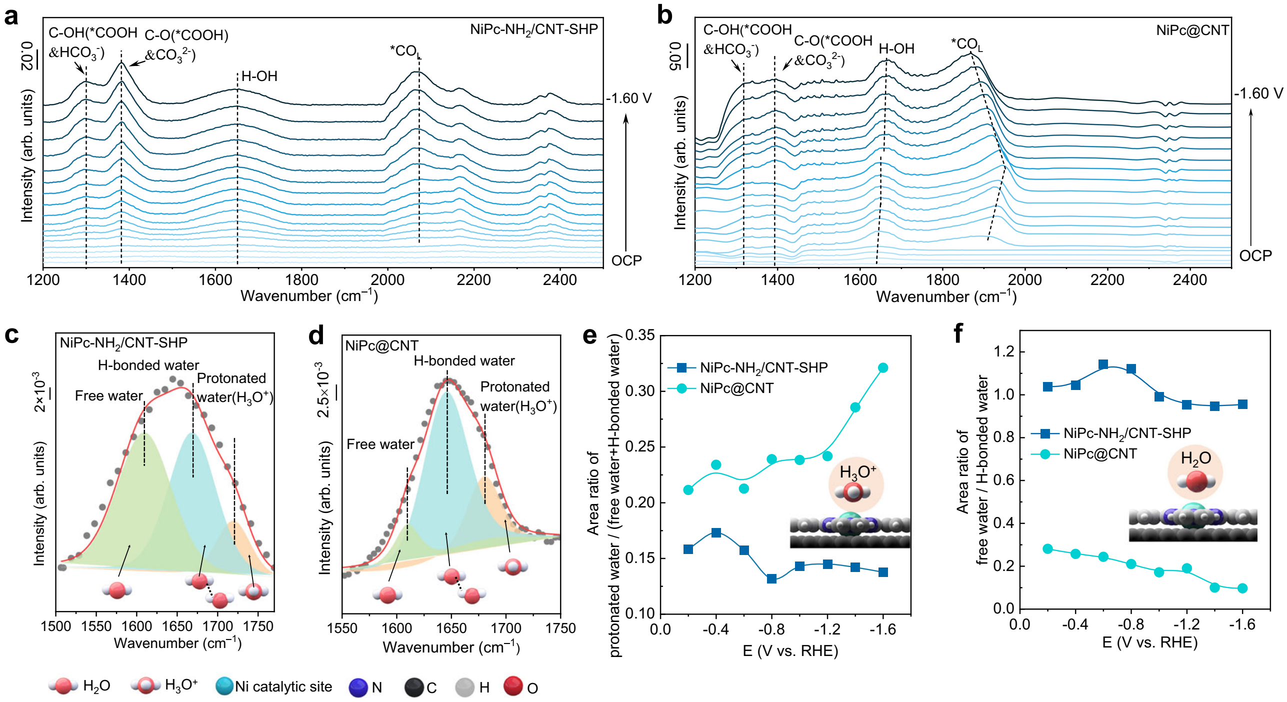

Fig. 3 | In-situ infrared spectroscopy of interface species. a In-situ infrared spectroscopy of NiPc-NH$_2$/CNT-SHP (without iR compensation). **b** In-situ infrared spectroscopy of NiPc@CNT (without iR compensation). ATR-SEIRAS of interfacial water on NiPc-NH$_2$/CNT-SHP (**c**) and NiPc@CNT (**d**) at −0.80 V in CO$_2$-saturated 0.5 M $K_2SO_4 + H_2SO_4$ (pH = 1). **e** Potential-dependent area ratio of protonated water / (H-bonded water + free water) on NiPc@CNT (cyan) and NiPc-NH$_2$/CNT-SHP (blue) in CO$_2$-saturated 0.5 M $K_2SO_4 + H_2SO_4$ (pH = 1, without iR compensation). **f** Potential-dependent area ratio of free water / H-bonded water on NiPc@CNT (cyan) and NiPc-NH$_2$/CNT-SHP (blue) in CO$_2$-saturated 0.5 M $K_2SO_4 + H_2SO_4$ (pH = 1, without iR compensation). The error bars represent the standard deviation of three independent measurements. Source data are provided as a Source Data file.

amine species (Supplementary Fig. S30). However, upon the introduction of acidic electrolyte, a distinct peak emerged at approximately 402.1 eV under open-circuit potential, which can be assigned to the $-NH_3^+$ species[35–37]. This observation aligns well with our initial hypothesis. Furthermore, when applying potentials ranging from 0 to −1.6 V *vs.* RHE, the $-NH_3^+$ species remained clearly visible, indicating that the amino cation is stably maintained in the strongly acidic environment and plays a role in modulating the interfacial environment during electrochemical CO$_2$ reduction.

Subsequently, in view of the above differences in selectivity, we performed in situ attenuated total reflection surface-enhanced infrared absorption spectroscopy (ATR-SEIRAS) in a CO$_2$-saturated 0.5 M $K_2SO_4 + H_2SO_4$ solution (pH = 1) to obtain detailed molecular vibration information at the catalyst interface[38]. The peak at 1298 cm^{-1} is attributed to the OH-deformation of the *COOH intermediate and interfacial bicarbonate species[39,40], while a strong peak at 1381 cm^{-1} is contributed to the C − O stretching of *COOH intermediate and interface carbonate[41,42], where the *COOH intermediate is crucial for the electrochemical reduction of CO$_2$ to CO. The formation of (bi)carbonate originates from the alkaline environment at the catalyst interface[38]. Furthermore, another important peek at 2064 cm^{-1} belongs to the linearly bonded *CO (*CO$_L$) on the Ni atom of NiPc-NH$_2$/CNT-SHP[43,44], and its signal intensity enhances with the tested potential, in line with that of the *COOH intermediate (Supplementary Fig. S31), indicating that *CO$_L$ and *COOH are essential intermediates for CO$_2$ electrochemical reduction to CO. Similar spectral features were observed for NiPc@CNT. However, NiPc@CNT displays a lower *CO$_L$ wavenumber (~1948 cm^{-1}) compared with NiPc-NH$_2$/CNT-SHP, indicating stronger CO adsorption[39,43,44], which is likely due to the modification of the Ni electronic structure by different peripheral functional groups on the molecular catalyst[45], leading to variations in CO adsorption strength at different sites. On the other hand, NiPc@CNT exhibited a noticeable shift in H$_2$O-related peak positions with the tested potential in acidic conditions (Fig. 3b), whereas this was not observed under neutral conditions (Supplementary Fig. S32).

To elucidate this phenomenon, we analyzed the bending vibration of H−O−H (1500–1750 cm^{-1}), which was deconvoluted into three peaks: ~1620 cm^{-1} (free water)[46,47], ~1680 cm^{-1} (H-bonded water)[48,49], and ~1715 cm^{-1} (protonated water, H_3O^+) (Fig. 3c, d, and Supplementary Figs. S33, S34)[50]. Compared to NiPc-NH$_2$/CNT-SHP (Fig. 3c), NiPc@CNT exhibited a significantly higher proportion of H_3O^+ and a reduced fraction of free water (Fig. 3d). The area ratio of protonated water to the sum of free and H-bonded water was consistently lower for NiPc-NH$_2$/CNT-SHP than for NiPc@CNT and increased with applied potential (Fig. 3e). The cation-dependent variations in the H−O−H stretching region (3000–3800 cm^{-1}) are consistent with those observed in the bending region (1500–1750 cm^{-1}), as shown in Supplementary Fig. S35. At −1.6 V *vs.* RHE, NiPc@CNT displayed an area ratio approximately 2.3 times higher than NiPc-NH$_2$/CNT-SHP, indicating greater H_3O^+ infiltration into the catalyst interface, thereby reducing FE$_{CO}$ (Fig. 2b) and weakening *COOH signal intensity.

Moreover, NiPc-NH$_2$/CNT-SHP exhibited a significantly higher ratio of free water to H-bonded water compared to NiPc@CNT, reaching ~9.8 times at −1.6 V *vs.* RHE (Fig. 3f). In contrast, NiPc@CNT showed a decreasing trend with applied potential, likely due to H_3O^+ competition (Fig. 3e). Conversely, NiPc-NH$_2$/CNT-SHP maintained a stable ratio value of ~1.0, suggesting that the long-chain hydrophobic groups effectively manage the interfacial water, disrupt the water network, and promote free water infiltration into the electric double layer, facilitating CO$_2$RR[35]. This enhanced interfacial water management accelerates the kinetics of adsorbed CO$_2$ conversion[39], corroborating the superior catalytic activity of NiPc-NH$_2$/CNT-SHP compared to NiPc@CNT (Fig. 2c).

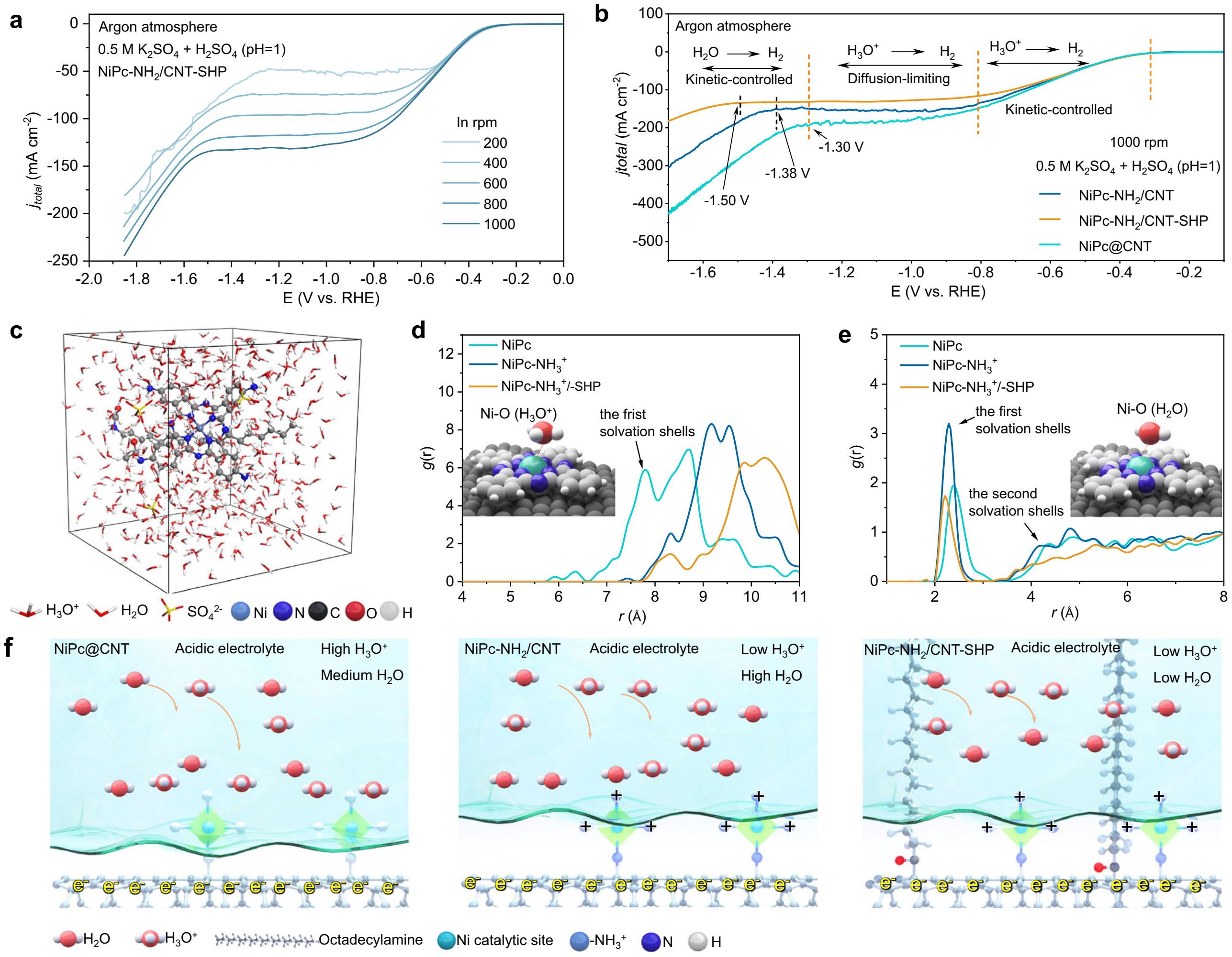

Fig. 4 | Mechanism analysis of interfacial water influence. **a** LSV curves of NiPc-NH_2/CNT-SHP in Ar-saturated electrolyte of 0.5 M $K_2SO_4 + H_2SO_4$ (pH = 1) under varied rotating speed (without iR compensation). **b** A comparison of NiPc-NH_2/CNT-SHP, NiPc-NH_2/CNT, and NiPc/CNT at 1000 rpm (without iR compensation). **c** A typical model of NiPc-NH_2/-SHP for MD simulations, red: O, white: H, blue: N, black: C, yellow: S, light blue: Ni. **d** Radial distribution functions (*g(r)*) of H_3O^+ surrounding the Ni center for NiPc, NiPc-NH_3^+ and NiPc-NH_3^+/-SHP. **e** *g(r)* of H_2O surrounding the Ni center for NiPc, NiPc-NH_3^+ and NiPc-NH_3^+/-SHP. **f** Schematic presentation of water species distribution on the surface of NiPc@CNT, NiPc-NH_2/CNT, and NiPc-NH_2/CNT-SHP.

To validate the above findings, we further measured the polarization curves of a rotating disk electrode (RDE) coated with NiPc-NH_2/CNT-SHP (Fig. 4a), NiPc-NH_2/CNT, and NiPc@CNT (Supplementary Fig. S36) at different rotating speeds in an Ar-saturated 0.5 M $K_2SO_4 + H_2SO_4$ (pH = 1). The onset potentials for HER were similar across all catalysts. A current density plateau, indicative of HER from diffusion-limited hydronium reduction, was observed on all electrodes (Fig. 4a, and Supplementary Fig. S37). However, NiPc-NH_2/CNT-SHP exhibited a lower plateau current density than NiPc@CNT, likely due to attenuated H_3O^+ mass transport to the cathode surface (Fig. 3d)[24]. The linear fitting of the plateau current density (j_{plateau}) using the Levich equation (Supplementary Figs. S38, 39) reveals an approximately 40% decrease in the H_3O^+ diffusion coefficient (D_{H3O^+}) for NiPc-NH_2/CNT-SHP compared to NiPc@CNT. The kinetic current densities were subsequently calculated using the Koutecký–Levich equation, showing a ~ 2.5-fold decrease in HER activity from ~990 mA cm^{-2} for NiPc@CNT to ~400 mA cm^{-2} for NiPc-NH_2/CNT-SHP (Supplementary Fig. S38). In addition, linear fitting of the total current density (j_{plateau}) against $\omega^{1/2}$ indicates that NiPc-NH_2/CNT-SHP exhibits slower interfacial water reduction kinetics than both NiPc@CNT and NiPc-NH_2/CNT. Collectively, the RDE results demonstrate that the presence of hydrophobic domains and $-NH_3^+$ functionalities effectively suppress both hydronium and water reduction, thereby promoting selective CO_2 electroreduction in acidic media, in line with the trends observed in the in situ ATR-SEIRAS spectra.

Furthermore, for NiPc-NH_2/CNT-SHP at 1000 rpm, a significant increase in current density for H_2O reduction was observed at −1.50 V *vs.* RHE, whereas this process commenced at −1.38 V and −1.30 V *vs.* RHE for NiPc-NH_2/CNT and NiPc@CNT, respectively. This shift illustrates the suppressed H_2O reduction in NiPc-NH_2/CNT-SHP (Supplementary Fig. S39), supporting its high FE_{CO} under high current density conditions, which can be attributed to the designed hydrophobic interfacial environment. The hydrophobic structure also demonstrated high stability (Supplementary Fig. S40).

To simulate the microenvironment surrounding our catalysts, we conducted molecular dynamics (MD) simulations (see Methods for details). We examined the influence of different interfacial environments and varying concentrations of charged species (namely K^+, H^+) on the transport of H_2O. In the present case, we paid particular attention to the distribution of H_2O and H_3O^+ relative to the Ni catalyst center (Fig. 4c, and Supplementary Figs. S33, 34). We propose that in situ-generated NH_3^+ at the catalyst periphery would repel other cationic species, while the long-chain hydrophobic molecules would hinder interfacial water adsorption. Such effects might lead to reduced accumulation of H_3O^+ and H_2O near the catalytic center, thereby alleviating competing HER.

To assess the distribution of H_2O species around the solvated catalysts, we computed radial distribution functions, *g(r)*, to analyze H_3O^+ proximity to the Ni catalytic center (Supplementary Figs. S42, 43, Fig. 4d). The NiPc-NH_3^+ and NiPc-NH_3^+/-SHP (octadecylamine) lines showed that H_3O^+ tends to reside beyond 7.7 Å from the Ni center compared with that of NiPc (5.7 Å), which could be attributed to coulombic repulsion with the positively NH_3^+ present on the molecules. It leads to the electrolytic H_3O^+ far away from the Ni center, which is consistent with the result of ATR-SEIRAS (Fig. 3e). Meanwhile, NiPc-NH_3^+ is primarily distributed in a higher 8.5–10.0 Å range than that of NiPc (7.5–9.0 Å), but NiPc-NH_3^+/-SHP showed the highest peak position of 9.5–11.0 Å. These data suggest that the combination of long-chain hydrophobic molecules and NH_3^+ groups further inhibit the approach of protonated water, thereby supporting the enhanced CO_2RR selectivity of NiPc-NH_2/CNT-SHP. Meanwhile, further density functional theory (DFT) calculations suggest that H_3O^+ could promote a Volmer-type reaction at the imine nitrogen site, leading to reduced catalyst stability and activity (Supplementary Figs. S44, 45), thereby highlighting the importance of interfacial exclusion of protonated water species.

Furthermore, we also analyzed the distribution of H_2O near the central Ni in NiPc, NiPc-NH_3^+, and NiPc-NH_3^+/-SHP (Fig. 4e), which shows a peak at ~2.3 Å, representing the first solvation shells. It is worth noting that the strength of the first solvation shell of NiPc-NH_3^+/-SHP is lower than that of NiPc-NH_3^+ and NiPc, suggesting that less H_2O exists at the interface of NiPc-NH_3^+/-SHP and the distribution of interfacial water was affected by the long-chain hydrophobic groups, consistent with the result of ATR-SEIRAS (Supplementary Fig. S47). NiPc–NH_3^+ narrows the water distribution range around NiPc from 2.0–3.2 Å to 2.0–2.8 Å, yielding a higher intensity. This implies that -NH_3^+ not only influence H_3O^+, but also modulate the distribution of H_2O (excluding H_3O^+) at the interface. It is attributed to the positively charged group exhibiting an increased propensity for hydrogen bonding with water, thereby enhancing their affinity for water, consistent with our previous assumptions, indicating the important role of secondary introduction of hydrophobic long chains.

Interestingly, the second *g(r)* peak, representing the second solvation shell, is located at ~4.2 Å for both NiPc and NiPc-NH_3^+, whereas no peak is observed in the case of NiPc-NH_3^+/-SHP. This finding further suggests that long-chain hydrophobic groups not only alter the distribution of interfacial water but also disrupt the hydrogen bonding network of water farther from Ni (the second solvation shell), consistent with ATR-SEIRAS (Fig. 3e). The broken hydrogen bonding produces a more hydrophobic environment, which allows CO_2 to reside near the catalytic site and be reduced more readily[24]. On the other hand, the broken hydrogen bonding inhibits proton jumping from H_3O^+ to the catalyst via the Grotthuss mechanism[24], allowing more free water to enter (Fig. 3c), which further facilitates CO_2RR and suppresses HER (Fig. 2b)[38]. In general, our MD simulations agree well with these RDE and ATR-SEIRAS results. Combining all our analyses, the acidic CO_2RR performance on NiPc-NH_2/CNT-SHP catalyst can be convincingly ascribed to the advantageous synergies between -NH_3^+ groups and long-chain hydrophobic modifications in optimizing the interfacial microenvironment. This effects likely reduce H_3O^+ and H_2O coverage at the Ni catalytic unit (Fig. 4f), enrich CO_2 near the interface, and thus improve selectivity under high current operation (Fig. 2c). Given the outstanding performance of NiPc-NH_2/CNT-SHP in acidic CO_2RR, we proceeded to optimize it for evaluation in a PEM reactor.

Electrochemical performance test in acid PSE reactor and TEA analysis

To enable continuous CO production under acidic conditions in a practical system, we constructed a PEM reactor incorporating NiPc-NH_2/CNT-SHP as the cathode. Given the operating conditions in a flow cell, 0.05 M K_2SO_4 + 0.05 M H_2SO_4 was initially used as the anolyte to mitigate (bi)carbonate precipitation. As potassium ions migrate across the membrane in hydrated form, they alter the catalyst's local environment, increasing alkalinity at the cathode interface.[11], However, CO production remained minimal (Supplementary Fig. S48), likely due to high proton flux at the catalyst/membrane interface[51]. Increasing the K^+ concentration (0.5 M K_2SO_4 + 0.05 M H_2SO_4) slightly improved FE_{CO} (Supplementary Fig. S49), but salt precipitations were observed in the flow channels after more than ten hours of testing (Supplementary Fig. S50), likely due to the local generation of high proton concentrations at the catalyst/membrane interface during the oxygen evolution reaction on the anode side. These protons will then be promptly transported across the PEM to the cathode side from the strong acid interface, which suppresses K^+ transport from the anolyte to the cathode, hindering the regulation of the interfacial environment for CO_2RR, a process distinct from the interfacial environment of the catalyst in the acidic environment of the flow cell. The low FE_{CO} in the PEM reactor prompted us to establish a strong acid buffer interval to mitigate the impact of the strong acid interface on CO_2RR performance.

Instead of a conventional PEM reactor design, we developed a PSE reactor (Supplementary Figs. S51, 52) featuring two chambers separated by a PEM, where a conductive anionic PSE layer functions to (1) minimize *iR*-drop between the cathode and anode, (2) transfer protons while maintaining an acidic interfacial environment (Fig. 5a), (3) alleviate the strong-acid interface effect on CO_2RR performance. The system employs NiPc-NH_2/CNT-SHP on a gas diffusion layer (GDL) as the cathode and IrO_2-coated titanium mesh as the anode. The pure CO_2 was continuously supplied for the electrochemical reduction of CO_2 to CO. Meanwhile, the anode chamber was circulated with 0.5 M H_2SO_4 for OER, which can produce hydrogen protons. These protons will then be transported through the membrane and PSE layer to the cathode. They interact with diffused cations, regulating the local catalytic environment at the catalyst/PSE interface to facilitate CO generation. Additionally, bicarbonate at the catalyst/PSE interface reacts with protons to regenerate CO_2, mitigating salt deposition and carbon loss. Protons produced by water oxidation at the anode enter the middle chamber to balance the charge that has been spent.

The I–V curve of our PSE reactor flowing 0.1 M K_2SO_4 + 0.01 M H_2SO_4 solution in the PSE layer was plotted in Fig. 5b, where a high-concentration salt solution can be used. In contrast, we use the low salt concentration to mitigate salt precipitation during long-term testing for practical demonstrations. The PSE reactor's cell voltage progressively rose as the total current density increased, which achieved a current density of 300 mA cm^{-2} at the cell voltage of ~3.96 V. In contrast, the reactor without the PSE layer exhibited higher cell resistance (Supplementary Fig. S53b), leading to increased cell voltage at the same current (Fig. 5b). Owing to the bubbles generated from the anode disturbing the membrane, an apparent fluctuation was found in the constant current test of the PSE reactor without conductive solid electrolyte (Supplementary Fig. S54b). With the PSE reactor, NiPc-NH_2/CNT-SHP achieved a total current density of 150 mA cm^{-2} at ~3.37 V, significantly lower than ~5.11 V in the absence of the PSE layer.

The strong acidity at the catalyst/PSE interface led to slightly lower FE_{CO} in the PSE reactor compared to the non-PSE system at currents below 120 mA cm^{-2} (Fig. 5c). This discrepancy can also be mitigated by increasing the salt concentration (Supplementary Fig. S55). However, as the test current increases, the increased K^+ facilitates the enhancement of interfacial alkalinity, resulting in comparable FE_{CO} (~ 98%) between both systems at 120 mA cm^{-2} (Fig. 5d). Due to the lack of solid electrolyte support, the gas generated by the anode fluctuates on the electrical signal, thus the constant current test stops at 150 mA cm^{-2} without PSE reactor (Fig. 5b). Notably, FE_{CO} remained above 90% across a wide current range (100–300 mA cm^{-2}), with NiPc-NH_2/CNT-SHP achieving j_{CO} of ~148.38 mA cm^{-2} at ~3.37 V in the acidic PSE reactor, compared to ~4.60 V without PSE. At 3.96 V, j_{CO} reached 295.26 mA cm^{-2} (Fig. 5e).

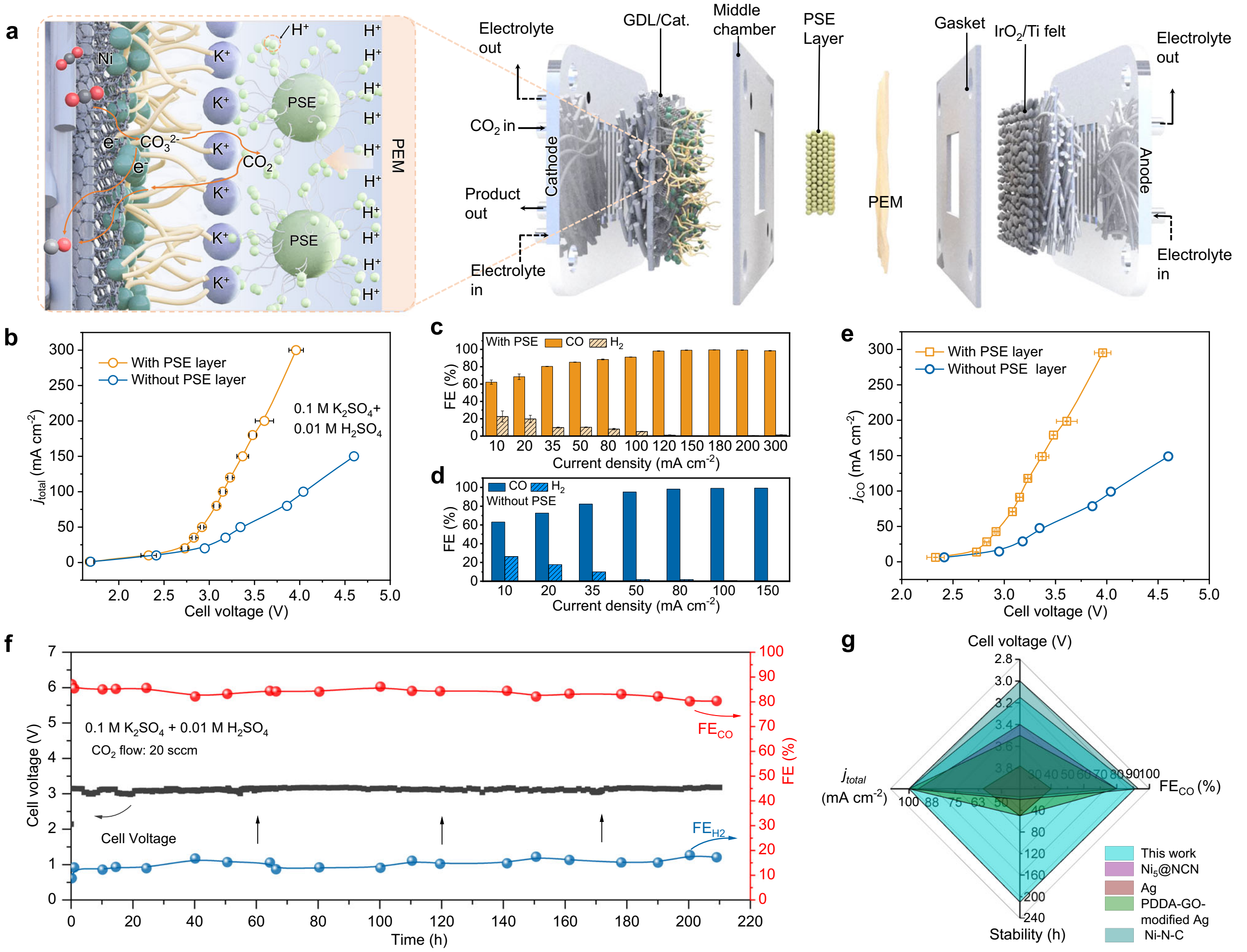

Fig. 5 | Electrochemical performance test in the acid PEM-PSE reactor. **a** Schematic illustration of reducing CO$_2$ to CO in our acid PSE reactor. **b** I–V curve (without iR compensation), **c, d** FE$_{CO}$, and **e** j_{CO} (without iR compensation) for CO$_2$ RR using the reactor with (Resistance: 2.40 ± 0.44 Ω) or without (Resistance: 9.40 ± 1.37 Ω) PSE layer. **f** The chronopotentiometry stability test of the acid PSE reactor by directly flowing 0.1 M K$_2$SO$_4$ + 0.01 H$_2$SO$_4$ solution (pH = 2.27 ± 0.22 Ω) in the middle chamber at the current density of 100 mA cm^{-2} and the corresponding FE$_{CO}$, black arrow: renewing electrolyte. **g** Comparison of our work with other relevant studies in terms of j_{total}, cell voltage, stability, and FE$_{CO}$ for full-cell acidic CO$_2$RR. The error bars represent the standard deviation of three independent measurements. Source data are provided as a Source Data file.

Electrolysis stability is one of the most crucial yet challenging components for evaluating practical applications in acidic conditions. Benefiting from the NiPc-NH$_2$/CNT-SHP, which features a stable Ni molecular site, a superhydrophobic interface, and a reliable design, our PSE reactor exhibits long-term stability in producing CO under acidic conditions. Even though a low concentration of K$^+$ was used, a slight salt was also found on the back of the electrode. Consequently, the serpentine channel was rinsed with deionized water every 40 h, and the cathodic electrolyte was refreshed approximately every 60 h under a sealed state. This procedure prevents salt precipitation from obstructing the channel and ensures adequate K$^+$ availability for CO$_2$ reduction reactions (CO$_2$RR). Notably, no organic products were detected in the liquid electrolyte after the 20-hour stability test, indicating the absence of liquid-phase products (Supplementary Fig. S56) and confirming the high stability of the PSE. The PSE reactor stability was evaluated by maintaining a 100 mA cm^{-2} current density for 200 h with a high FE$_{CO}$ above 80%. The whole-cell voltage was maintained at ~3.17 V (Fig. 5f). Following the 200 h test, the stability of the catalyst was confirmed by XPS, XAS, TEM, and contact angle measurements (Supplementary Figs. S57–60). Compared with the original PSE (Supplementary Fig. S52), no significant morphological changes were observed in the PSE after a 200 h test (Supplementary Figs. S61a, b), further confirming the structural stability of the PSE. Here we also conducted additional experiments to demonstrate that heat treatment significantly enhances energy efficiency, especially under high operational current densities (Supplementary Fig. S62). Additionally, NiPc-NH$_2$/CNT-SHP achieved a high j_{CO} of 210.45 mA cm^{-2} at a cell voltage of 4.17 V in alkaline conditions and exhibited long-term stable operation at 50 and 100 mA cm^{-2} (Supplementary Figs. S63–65), further underscoring its superior performance. Consequently, the NiPc-NH$_2$/CNT-SHP catalyst offers extended operational time, comparable cell voltage, and FE$_{CO}$ relative to existing reports on CO$_2$RR under acidic conditions (100 mA cm^{-2}, Supplementary Table S4, Fig. 5g)[11,20,23,52], underscoring the advanced nature of this catalyst design.

Based on the electrochemical performance of our acidic PSE reactor system for CO$_2$ electrochemical reduction, we conducted a techno-economic analysis (TEA) to evaluate its economic viability and adaptability, adapting previously reported methodologies. Several process assumptions were made based on current feedstock prices and electrolyzer performance, with a sensitivity analysis accounting for potential future fluctuations in these parameters. The study of CO production costs indicates a total system cost range of approximately US$327.68 to US$351.91 per ton of CO at current densities between 100 and 300 mA cm^{-2} (Supplementary Fig. S66a). Taking 100 mA cm^{-2} as an example, the major cost contributors are as follows: electrolyzer and installation ($43.75 per ton of CO), balance-of-plant (BOP) components ($9.22 per ton of CO), electricity consumption ($198.47 per ton of CO), input chemicals ($63.41 per ton of CO), and other operational expenses ($31.51 per ton of CO). Furthermore, a detailed global sensitivity analysis shows that generation costs are highly sensitive to variations in electricity prices (Supplementary Fig. S66b, ranging from $0.02 to $0.06), cell voltages (ranging from 2.0 to 5.0 V), FE_{CO} (ranging from 100 to 50%), and current density (400 to 20 mA cm^{-2}). This is because electricity prices are directly related to operating costs, and cell voltages are tied to the amount of electricity consumed. The Faradaic efficiency of products and current density affect the size and capital cost of electrolyzers for producing 1 ton of CO (Supplementary Note 1). Other parameters, such as stack cost, exert a moderate effect on costs. Overall, developing strategies to prevent declines in FE_{CO} and current density under specific voltage changes, as well as monitoring electricity policy and price fluctuations, will be crucial for ensuring the economic feasibility of acidic CO_2RR in the future.

Discussion

A nickel-based heterogeneous molecular electrocatalyst (NiPc-NH_2/CNT-SHP) featuring -NH_2 functional groups and grafted long-chain hydrophobic molecules has been successfully synthesized. Under acidic conditions, the -NH_2 group is in situ protonated to form -NH_3^+, facilitating acidic CO_2RR at high current. The designed catalyst exhibited good stability, activity, and selectivity for the electrochemical reduction of CO_2 to CO under acidic conditions, outperforming its counterparts lacking hydrophobic and amino groups. In acidic electrolytes, the catalyst achieves a FE_{CO} of nearly 100%, a current density (j_{CO}) of 426 ± 14 mA cm^{-2}, and a CO_2 utilization rate of 76%. In comparison, the maximal FE_{CO} of above 99% and j_{CO} of 390 ± 7 and 414 ± 40 mA cm^{-2} can be achieved in alkaline and neutral electrolytes, respectively. MD simulations, RDE test, in-situ ATR-SEIRAS and in-situ XPS proved that the positively charged -NH_3^+ and superhydrophobic interface disrupt the protonated water (H_3O^+)-rich network, influencing the migration of free water, H-bonded water, and H_3O^+. This disruption inhibits H_3O^+ invasion and optimizes the distribution of free water, thereby enhancing selective CO_2RR performance under acidic conditions. Notably, NiPc-NH_2/CNT-SHP demonstrated outstanding FE_{CO} (> 80%) and operational stability (>200 h) at industrially relevant current densities in an acidic PEM-PSE reactor, which would be a promising demonstration of the use of renewable electricity for the continuous generation of CO through CO_2 reduction at a more feasible scale.

Methods

Chemicals

Ethanol (CH_3CH_2OH, ≥99.7%), nickel chloride ($NiCl_2$, ≥99%), 1-pentanol (≥99.0%), 1, 8-diazabicyclo[5.4.0]undec-7-ene (DBU, ≥98.0%), N, N-dimethylformamide (DMF, ≥99.9%), potassium hydroxide (KOH, ≥85.0%), hydrochloric acid (HCl, 36% ~ 38%), potassium bicarbonate ($KHCO_3$, ≥99.9%), sulfuric acid (H_2SO_4, ≥99.8%), thionyl chloride ($SOCl_2$, ≥99%) were all purchased from Sinopharm Chemical Reagent Co., Ltd. Nickel phthalocyanine (NiPc, ≥85%) was purchased from Aladdin chemical company. Carboxyl-functionalized carbon nanotube (CNT-COOH, ≥95%), graphitized carbon nanotube (CNT), and octadecylamine (≥90%) were purchased from Macklin Chemical Company. 4-Aminophthalonitrile (≥98.0%) was purchased from Bidepharm Chemical Company. High-purity carbon dioxide gas (CO_2, 99.999%) and high-purity argon (Ar, 99.999%) were purchased from Jiangsu SoPo Gas Co., Ltd. (China). Millipore water (18.2 MΩ·cm) was used throughout all experiments.

Synthesis of amino-substituted nickel phthalocyanine

NiPc–NH_2 was synthesized by dissolving 8 mmol 4-aminophthalonitrile, 1 mmol $NiCl_2$, and 2 mL 1,8-diazabicyclo[5.4.0]undec-7-ene in 60 mL 1-pentanol under ultrasonic treatment. After Ar purging, the solution was sealed in a 100 mL Teflon-lined autoclave and heated at 180 °C for 8 h. During the solvothermal reaction, base-promoted cyclization of phthalonitrile yielded crude amino-substituted nickel phthalocyanine. The product was sequentially treated in 1 M HCl and 1 M NaOH at 90 °C for 1 h each, filtered, washed with water, and purified via Soxhlet extraction (methanol) to afford pure NiPc–NH_2 as a dark green-blue solid.

Synthesis of NiPc-NH_2/CNT-SHP and NiPc-NH_2/CNT catalyst

Commercial carboxylated CNTs were vacuum-dried at 110 °C overnight. 200 mg of CNTs were dispersed in 40 mL $SOCl_2$ and 4 mL DMF, degassed, and refluxed at 70 °C for 24 h under Ar to yield acyl chloride-functionalized CNTs (CNT–COCl). The product was filtered, quenched with 1 M KOH to remove residual $SOCl_2$, washed with DMF, and then vacuum-dried. Subsequently, 200 mg of CNT–COCl was dispersed in 200 mL DMF and sonicated for 30 min, followed by the addition of 40 mg NiPc–NH_2 and further sonication. After degassing, the mixture was refluxed at 90 °C for 12 h under argon. Then, 3 g of octadecylamine was added, and the mixture was refluxed for another 12 h. The resulting NiPc–NH_2/CNT–SHP was collected by filtration, washed with DMF, ethanol, and water, and dried under vacuum. NiPc–NH_2/CNT was prepared identically but without octadecylamine.

Synthesis of NiPc@CNT catalyst

Commercial NiPc (40 mg) was dispersed in 100 mL of DMF and sonicated for 30 min. Separately, graphitized CNTs (200 mg) were dispersed in 100 mL of DMF and sonicated for 30 min. The two solutions were mixed under vigorous stirring, followed by continuous stirring for 24 h. The resulting NiPc@CNT was collected by vacuum filtration, washed with DMF and ethanol until the filtrate was colorless, and dried under vacuum.

Synthesis of NiPc@CNT-SHP catalyst

200 mg of CNT-COCl was dispersed in 200 mL of DMF and sonicated for 30 min. Subsequently, 40 mg of NiPc was added, followed by an additional 30 min of sonication. The mixture was degassed and refluxed at 90 °C under an argon atmosphere for 12 h. Then, 3 g of octadecylamine was added, and the reaction was continued under reflux at 90 °C for an additional 12 h. The resulting NiPc@CNT-SHP was collected by filtration, washed sequentially with DMF, ethanol, and water, and dried under vacuum.

Flow cell test

3 mg of samples, 1 mL of ethanol and 30 µL of Nafion (5 wt%) solution were mixed and ultrasonically treated for 1 h to obtain the ink solution. The obtained homogeneous ink was airbrushed onto 1×3 cm^2 hydrophobic carbon paper (Sigracet 28 BC gas-diffusion layer) to achieve a loading of 1 mg cm^{-2}, and then dried overnight at 60 °C. An Ag/AgCl electrode (3.5 M KCl, The Ag/AgCl reference electrode was calibrated in 0.5 M H_2SO_4 under H_2-saturated conditions using two Pt foil electrodes) and a Pt electrode were chosen as the reference (reaction area: 1 cm^2) and counter electrodes, respectively. All potentials from the three-electrode experiments were converted to versus RHE with 80% iR correction by the following Eq. (1):

$$E(\upsilon s.\mathrm{RHE}) = E\left(\upsilon s.\mathrm{Ag/AgCl}\right) + 0.2046\,\mathrm{V} + 0.059 \times \mathrm{pH} - iRu \qquad (1)$$

where i is the current and Ru is the solution resistance. The electrochemical performance of the samples was measured using an electrochemical workstation (Shanghai, CHI1140C). The gas products were analyzed using online gas chromatography (GC-2030; Shimadzu) equipped with a thermal conductivity detector (TCD) and a flame ionization detector (FID). Liquid products were detected using ^1H NMR spectroscopy with DMSO as an internal standard. Each cathode electrode was activated by cyclic voltammetry for 20 min before the constant current test. In alkaline and neutral conditions, 1 M KOH (50 mL) and 1 M $KHCO_3$ (50 mL) were used as the cathode and anode electrolytes, respectively. In acidic conditions, 0.5 M K_2SO_4 (pH=1) was used as the cathode electrolyte and 0.5 M H_2SO_4 (50 mL) was used as the anode electrolyte. Furthermore, the pH of 3 M KCl (50 mL) was adjusted to 0.4 using concentrated sulfuric acid, which was used as the cathode electrolyte, and 0.5 M H_2SO_4 (50 mL) was used as the anode electrolyte. Before the electrochemical test, the electrolyte was saturated with argon gas for 30 min. The electrolyte was circulated through the cathodic and anodic chambers using a peristaltic pump at rates of 10 mL min^{-1} and 40 mL min^{-1}, respectively. In all flow cell measurements, the test potential was corrected for 80% ohmic resistance. The cell resistances (R) were measured by electrochemical impedance spectroscopy (EIS) under open-circuit voltage. The flow rate of inlet CO_2 gas through the gas chamber was controlled to be 2 ~ 25 mL min^{-1} using a 100-sccm-range MFC, and a soap film flowmeter measured the outlet flow rate. The electrochemically active surface area (ECSA) and electrochemical impedance spectroscopy (EIS) were tested in an H-type cell by an electrochemical workstation (Shanghai, CHI760e). The cathodic electrolyte is CO_2-saturated 0.5 M $KHCO_3$, and the anodic electrolyte is 0.5 M $KHCO_3$. The ECSA experiment was carried out on a glassy carbon electrode (3.0 mm in diameter) at the non-CO_2 Faradaic efficiency potential. The ECSA is proportional to the C_{dl} value. The loading of the electrocatalyst was 0.2 mg cm^{-2}. The EIS experiment was conducted at a potential of −0.60 V *vs*. RHE.

Porous solid electrolyte reactor test

Electrochemical measurements were performed on a BioLogic VSP-3e workstation. The PSE reactor featured a NiPc-NH_2/CNT-SHP catalyst coated on a 1 cm^2 gas diffusion layer (GDL) as the cathode. A 0.25 mm PTFE gasket with a 1.0 cm^2 window and an anion exchange membrane (AEM) was positioned between the cathode and the solid electrolyte. An IrO_2/Ti mesh served as the anode, separated from the solid electrolyte by a Nafion 117 proton exchange membrane. The anode compartment was supplied with 0.5 M H_2SO_4 (50 mL) at a flow rate of 1.0 mL min^{-1} using a peristaltic pump, and the 0.01 M K_2SO_4 (50 mL) was used as the electrolyte in the middle chamber to reduce resistance. The central chamber contained a 2.5 × 2.5 cm^2 window filled with Dowex 50 W X8 (H^+ form), serving as the porous solid electrolyte. During CO_2RR tests, CO_2 gas was delivered to the cathode at a rate of 20 mL min^{-1} via a mass flow controller (Alicat). Prior to measurements, the cell was conditioned at a low current for ~20 min to stabilize the voltage and product selectivity.

Acid membrane electrode assembly electrolytic cell test

Electrochemical measurements were performed using a Bio-Logic VMP3e workstation. The cell assembly included a 0.25 mm polytetrafluoroethylene gasket with a 1.0 cm^2 window, a NiPc–NH_2/CNT–SHP catalyst coated on a 1 cm^2 GDL (1 mg cm^{-2}) as the cathode, and a commercial IrO_2 catalyst air-brushed onto Ti mesh (IrO_2/Ti) as the anode. The anode electrolyte consisted of either 0.05 M K_2SO_4 + 0.05 M H_2SO_4 (50 mL, stored at room temperature 25 °C) or 0.5 M K_2SO_4 + 0.05 M H_2SO_4 (50 mL, stored at room temperature 25 °C), delivered at 10 mL min^{-1} via a syringe pump. The anode and cathode chambers were separated by a Nafion HP membrane (20 μm). CO_2 gas was supplied to the cathode at a flow rate of 20 mL min^{-1} using a mass flow controller (100 sccm range).

Acid porous solid electrolyte reactor test

Electrochemical measurements were performed using a Bio-Logic VMP3e and a CHI 660e workstation, both equipped with a CHI 680c current booster. The cathodic compartment consisted of a stainless-steel chamber with a serpentine flow field and four ports: two for CO_2 gas circulation and two for electrolyte flow through a 1 mm thick middle chamber. A 0.5 mm silicone gasket with a 1.0 cm^2 window was used to ensure tight contact between the cathode and the solid electrolyte. The cathode received 20 mL min^{-1} of CO_2 (controlled by a 100 sccm Alicat MFC). IrO_2/Ti mesh served as the anode, separated from the solid electrolyte layer by a Nafion HP membrane (20 μm). The anode was supplied with 0.5 M H_2SO_4 (50 mL) at 2.0 mL min^{-1}, while the catholyte consisted of 0.1 M K_2SO_4 + 0.01 M H_2SO_4 (50 mL).

In situ electrochemical ATR-SEIRAS measurements

In situ ATR-SEIRAS measurements were performed using a Pike Veemax III ATR cell equipped with a single-reflection Si crystal coated with a thin Au film, operating in internal reflection mode. Spectra were collected on a Thermo Fisher, Nicolet^{TM} iS50 spectrometer (U.S.). A three-electrode configuration was employed, using NiPc–NH_2/CNT–SHP as the working electrode, Ag/AgCl as the reference, and Pt felt as the counter electrode. The electrolyte (0.5 M K_2SO_4+H_2SO_4, pH=1) was saturated with CO_2 for 30 min prior to measurement. Spectra were recorded over a potential range from the open-circuit potential (OCP) to −1.6 V *vs*. RHE.

In situ electrochemical XPS measurements

In situ X-ray photoelectron spectroscopy (XPS) was employed to monitor real-time changes in the surface chemical states during electrochemical CO_2 reduction. Prior to measurements, clean and flat electrode samples (diameter ≤10 mm) were prepared and mounted in an in situ electrochemical cell connected to an ultrahigh vacuum (UHV) chamber (base pressure $\leq 1\times10^{-9}$ mbar). XPS experiments were conducted using a Thermo Scientific K-Alpha system, and electrochemical control was achieved with a CorrTest workstation (CS350M). During the measurement, the electrochemical environment was precisely regulated, allowing for the stepwise acquisition of XPS spectral information (N 1*s*, C 1*s*) at different applied potentials. Particular attention was paid to shifts in binding energy, intensity variations, and the emergence of features in the XPS spectra to elucidate the interfacial processes occurring during operation.

Computational details

DFT and ab initio molecular-dynamics (AIMD, Supplementary Data 1) simulations were performed with the Vienna ab initio Simulation Package (VASP)[53] using projector augmented-wave (PAW) potentials[54] and a 400 eV plane-wave cutoff. Exchange–correlation was described by the PBE functional[55] within GGA and augmented by the DFT-D3 dispersion correction[56]. All calculations were spin-polarized, and Brillouin-zone integration employed a Γ-only k-mesh[57], suitable for the isolated-molecule cell. A cubic box of 20 × 20 × 20 $Å^3$ containing one NiPc unit was used. Geometry optimizations converged at 1×10^{-5} eV for energies and 0.01 eV $Å^{-1}$ for forces. AIMD simulations employed a Nosé–Hoover thermostat at 300 K with 1 fs time steps, setting H masses to those of deuterium[58]. Reaction barriers were obtained via the slow-growth enhanced sampling method[59].

Since explicit AIMD of bulk water is computationally prohibitive, we construct a·finite-radius water-droplet model that mimics the solvation environment of NiPc molecule and thus makes AIMD· tractable. In this approach, the outer tier of water molecules feel a Lennard-Jones-like repulsive force·so·that the water moleclules do not drift too far from the central Ni atom.

All molecular-dynamics (MD) simulations were carried out in the canonical (NVT) ensemble at 298.15 K with initial random velocities, each extending beyond 20 ps. Equations of motion were integrated via the velocity–Verlet algorithm with a 1 fs time step, and temperature was maintained by a Nosé thermostat (Q = 0.01). Covalent interactions (bonds, angles, and dihedrals) were described by the Universal Force Field, with partial charges from the QEq (spell out) method. Long-range electrostatics and van der Waals forces were treated by Ewald summation (accuracy = 0.001 kcal mol^{-1}) using a 12 Å cutoff under periodic boundary conditions.

All three systems were contained in 25× 25 × 25 Å cubic boxes. To maintain the density of liquid water, 478, 469, and 451 water molecules were added to the system 1 (NiPc), system 2 (NiPc-NH_3^+), and system 3 (NiPc-NH_3^+/-SHP), respectively. Since the electrolyte employed in the experiments was the acidic K_2SO_4 solution, all MD simulations were performed with H_3O^+, K^+ and SO_4^{2-} to maintain charge neutrality. To ensure a uniform H_3O^+ concentration, each system contained three H_3O^+ ions. In system 1, since the NiPc molecule is neutral, two SO_4^{2-} anions and one additional K^+ cation were added to maintain charge neutrality. In system 2, the protonated NiPc−NH_3^+ molecule carries three NH_3^+ groups, considering the three H_3O^+ ions in solution, three SO_4^{2-} anions were required for charge neutrality. System 3 (NiPc−NH_3^+/-SHP) was identical to system 2, except that an SHP molecule was positioned 4.2 Å from the Ni center.

Rotating disk electrode experiments

The diffusion limiting current of the reduction of hydronium ions was calculated according to Levich Eqs. (2–3)[60]:

$$i_{plateau} = 0.62nFAD^{\frac{2}{3}}\upsilon^{-\frac{1}{6}}c_{O,H^+}\omega^{\frac{1}{2}} \tag{2}$$

$$S = 0.62nFAD^{\frac{2}{3}}\upsilon^{-\frac{1}{6}}c_{O,H^+} \tag{3}$$

where n is the number of electrons transfer in the reaction, F is the Faraday constant (9.65×10^4 C mol^{-1}), A is the electrode surface area, D is the diffusion coefficient of hydronium ions, υ is the kinematic viscosity of electrolyte, c_{O,H^+} is the bulk concentration of hydronium ions, and ω is the rotating speed of the RDE (unit: rad s^{-1}), $i_{plateau}$ is the current. S is the linear fitting slope.

The kinetic current density can be obtained from the Koutecky-Levich Eq. (4):

$$\frac{1}{J_{tot}} = \frac{1}{J_k} + \frac{1}{J_{plateau}} \tag{4}$$

where j_{tot} is the total current density, j_k is the kinetic current density and $j_{plateau}$ is the diffusion limiting current density.

Evaluation of Faraday efficiency

The Faradic efficiency of the gas product was calculated by the following Eq. (5):

$$\mathrm{FE}_x = \frac{n_x \times F(C/mol) \times V(ml/\min) \times 10^{-6}(m^3/ml) \times \upsilon(vol\%) \times 1.013 \times 10^5(N/m^2)}{8.314(Nm/molK) \times T(K) \times I_{total}(C/s) \times 60(s/\min)} \tag{5}$$

n_x: the number of electrons required to produce a product molecule (H_2, CO = 2);

F: the Faradaic constant (96485 C mol^{-1});

V: the flow rate of CO_2 bubbling;

υ: the volume ratio of gas product calculated from the peak area of GC current signal;

T: 298.15 K;

I_{total}: the steady-state cell current (C/s).

Evaluation of partial current density

The partial current density of gas product was calculated by the following Eq. (6):

$$j_x = FE_x \times j_{total} \tag{6}$$

j_x: the partial current density (mA cm^{-2}) of gas product;

FE_x: the Faradic efficiency of the gas product;

j_{total}: the total current density (mA cm^{-2}).

Evaluation of TOF

The turnover frequency (TOF, s^{-1}) value of the gas product was calculated by the following Eq. (7):

$$TOF_x = \frac{FE_x \times j_{total}}{n_x \times F \times \omega \times m_{cat}/M_{ni}} \tag{7}$$

ω: the content of nickel (Ni) in the hybrid catalysts;

m_{cat}: the amount of the tested catalyst;

M_{ni}: the relative molecular weight of Ni.

Material characterizations

The morphologies of as-prepared samples were studied by using TEM (Japan, JEOL-2100F), HRTEM (Japan, JEOL-2100F), HAADF-STEM (FEI Titan) with energy dispersive X-ray spectroscopy (EDX), and SEM performed with a field-emission scanning electron microanalyzer (Hitachi S-4800 II, Japan). Furthermore, the atomic information of NiPc-NH_2/CNT-SHP was characterized using an FEI Themis Z transmission electron microscope operated at 200 kV and equipped with double spherical aberration (Cs) correctors. The physical structure information of the samples was analyzed using an X-ray diffractometer (XRD, Bruker AXS Company, Germany) equipped with monochromated Cu Kα radiation (λ = 1.54178 Å) and an XPS spectrometer (ESCA PHI500). The Ni amount loading of the catalysts was quantified by inductively coupled plasma mass spectrometry (ICP-MS, Agilent 7800). ^{1}H NMR spectroscopy was performed with a 500 MHz spectrometer.

X-ray absorption spectroscopy (XAS)

The sample was analyzed using XAS at the Shanghai Synchrotron Radiation Facility in China. The spectra were processed and analyzed by the software codes (Athena)[61,62].

Data availability

The data generated in this study are provided in the Supplementary Information and Source Data file. All data supporting the findings of this study are available within the paper and its Supplementary Information or from the corresponding authors upon request. Source data are provided with this paper.

References

1. Ding, J. et al. A tin-based tandem electrocatalyst for CO_2 reduction to ethanol with 80% selectivity. *Nat. Energy* **8**, 1386–1394 (2023).
2. She, X. et al. Pure-water-fed, electrocatalytic CO_2 reduction to ethylene beyond 1,000 h stability at 10 A. *Nat. Energy* **9**, 81–91 (2024).
3. Xia, C. et al. Continuous production of pure liquid fuel solutions via electrocatalytic CO_2 reduction using solid-electrolyte devices. *Nat. Energy* **4**, 776–785 (2019).
4. Hao, Q. et al. Nickel dual-atom sites for electrochemical carbon dioxide reduction. *Nat. Synth.* **1**, 719–728 (2022).
5. Gao, D. et al. Rational catalyst and electrolyte design for CO_2 electroreduction towards multicarbon products. *Nat. Catal.* **2**, 198–210 (2019).
6. Xie, K. et al. Eliminating the need for anodic gas separation in CO_2 electroreduction systems via liquid-to-liquid anodic upgrading. *Nat. Commun.* **13**, 3070 (2022).
7. Rabinowitz, J. A. & Kanan, M. A. The future of low-temperature carbon dioxide electrolysis depends on solving one basic problem. *Nat. Commun.* **11**, 5231 (2020).

8. O'Brien, C. P. et al. Single pass CO_2 conversion exceeding 85% in the electrosynthesis of multicarbon products via local CO_2 regeneration. *ACS Energy Lett*. **6**, 2952 (2021).
9. Gu, J. et al. Modulating electric field distribution by alkali cations for CO_2 electroreduction in strongly acidic medium. *Nat. Catal.* **5**, 268–276 (2022).
10. Qiao, Y. et al. Engineering the local microenvironment over Bi nanosheets for highly selective electrocatalytic conversion of CO_2 to HCOOH in strong acid. *ACS Catal.* **12**, 2357–2364 (2022).
11. Pan, B. et al. Close to 90% single-pass conversion efficiency for CO_2 electroreduction in an acid-fed membrane electrode assembly. *ACS Energy Lett.* **7**, 4224–4231 (2022).
12. Jiang, Z. et al. pH-universal electrocatalytic CO_2 reduction with ampere-level current density on doping-engineered bismuth sulfide. *Angew. Chem. Int. Ed.* **136**, e202408412 (2024).
13. Zheng, X. et al. Ir-Sn pair-site triggers key oxygen radical intermediate for efficient acidic water oxidation. *Sci. Adv.* **9**, eadi8025 (2023).
14. Lee, T. et al. Acidic CO_2 electroreduction for high CO_2 utilization: catalysts, electrodes, and electrolyzers. *Nanoscale* **16**, 2235–2249 (2024).
15. Chen, J. & Wang, L. Effects of the catalyst dynamic changes and influence of the reaction environment on the performance of electrochemical CO_2 reduction. *Adv. Mater.* **34**, 2103900 (2022).
16. Wu, W. et al. Addressing the carbonate issue: electrocatalysts for acidic CO_2 reduction reaction. *Adv. Mater.* **37**, 2312894 (2024).
17. Varela, A. S. et al. pH effects on the selectivity of the electrocatalytic CO_2 reduction on graphene-embedded Fe–N–C motifs: bridging concepts between molecular homogeneous and solid-state heterogeneous catalysis. *ACS Energy Lett.* **3**, 812–817 (2018).
18. Ringe, S. et al. Double layer charging driven carbon dioxide adsorption limits the rate of electrochemical carbon dioxide reduction on gold. *Nat. Commun.* **11**, 33 (2020).
19. Wang, M. et al. Hydrophobized electrospun nanofibers of hierarchical porosity as the integral gas diffusion electrode for full-pH CO_2 electroreduction in membrane electrode assemblies. *Energy Environ. Sci.* **16**, 4423–4431 (2023).
20. Li, H. et al. Tailoring acidic microenvironments for carbon-efficient CO_2 electrolysis over a Ni–N–C catalyst in a membrane electrode assembly electrolyzer. *Energy Environ. Sci.* **16**, 1502–1510 (2023).
21. Monteiro, M. C. O. et al. Efficiency and selectivity of CO_2 reduction to CO on gold gas diffusion electrodes in acidic media. *Nat. Commun.* **12**, 4943 (2021).
22. Li, Z. et al. Electron-rich bi nanosheets promote $CO_2^{\cdot-}$ formation for high-performance and pH-Universal electrocatalytic CO_2 reduction. *Angew. Chem. Int. Ed.* **62**, e202217569 (2023).
23. Liu, Z. et al. Acidic electrocatalytic CO_2 reduction using space-confined nanoreactors. *ACS Appl. Mater. Interfaces* **14**, 7900–7908 (2022).
24. Zhang, Q. et al. A covalent molecular design enabling efficient CO_2 reduction in strong acids. *Nat. Synth.* **3**, 1231–1242 (2024).
25. Chen, B. et al. Enhancement of mass transfer for facilitating industrial-level CO_2 electroreduction on atomic Ni-N_4 sites. *Adv. Energy Mater.* **11**, 2102152 (2021).
26. Yan, C. et al. Coordinatively unsaturated nickel–nitrogen sites towards selective and high-rate CO_2 electroreduction. *Energy Environ. Sci.* **11**, 1204–1210 (2018).
27. Adler, Z. et al. Hydrogen peroxide electrosynthesis in a strong acidic environment using cationic surfactants. *Precis. Chem.* **2**, 129–137 (2024).
28. Chen, K. et al. Ligand Engineering in Nickel Phthalocyanine to Boost the Electrocatalytic Reduction of CO_2. *Adv. Funct. Mater.* **32**, 2111322 (2022).
29. Huang, N. et al. A stable and conductive metallophthalocyanine framework for electrocatalytic carbon dioxide reduction in water. *Angew. Chem. Int. Ed.* **132**, 16587–16593 (2020).
30. Liu, S. et al. Elucidating the electrocatalytic CO_2 reduction reaction over a model single-atom nickel catalyst. *Angew. Chem. Int. Ed.* **59**, 798–803 (2020).
31. Yang, H. B. et al. Atomically dispersed Ni(i) as the active site for electrochemical CO_2 reduction. *Nat. Energy* **3**, 40–147 (2018).
32. Jiang, Z. et al. Molecular catalyst with near 100% selectivity for CO_2 reduction in acidic electrolytes. *Adv. Energy Mater.* **13**, 2203603 (2023).
33. Sheng, X. et al. Engineering the Ni-N-C catalyst microenvironment enabling CO_2 electroreduction with nearly 100% CO selectivity in acid. *Adv. Mater.* **34**, 2201295 (2022).
34. Yan, Z. et al. Improving the efficiency of CO_2 electrolysis by using a bipolar membrane with a weak-acid cation exchange layer. *Nat. Chem.* **13**, 33–40 (2021).
35. Zhong, Y. et al. An artificial electrode/electrolyte interface for CO_2 electroreduction by cation surfactant self-assembly. *Angew. Chem. Int. Ed.* **59**, 19095–19101 (2020).
36. Li, N. et al. Interfacial peroxidase-like catalytic activity of surface-immobilized cobalt phthalocyanine on multiwall carbon nanotubes. *RSC Adv.* **5**, 9374–9380 (2015).
37. Zhang, C. & Zhao, J. Effects of pre-corrosion on the corrosion inhibition performance of three inhibitors on Q235 Steel in CO_2/H_2S saturated brine solution. *Int. J. Electrochem. Sci.* **12**, 9161–9179 (2017).
38. Zhang, Z. et al. Probing electrolyte effects on cation-enhanced CO_2 reduction on copper in acidic media. *Nat. Catal.* **7**, 807–817 (2024).
39. Wang, Q. et al. Attenuating metal-substrate conjugation in atomically dispersed nickel catalysts for electroreduction of CO_2 to CO. *Nat. Commun.* **13**, 6082 (2022).
40. Wang, Z. et al. Identification of synergies in Fe, Co-coordinated polyphthalocyanines scaffolds for electrochemical CO_2 reduction reaction. *Nano Lett.* **24**, 3249 (2024).
41. Moradzaman, M. & Mui, G. Infrared analysis of interfacial phenomena during electrochemical reduction of CO_2 over polycrystalline copper electrodes. *ACS Catal.* **10**, 8049–8057 (2020).
42. Chen, J. et al. Promoting electrochemical CO_2 reduction via boosting activation of adsorbed intermediates on iron single-atom catalyst. *Adv. Funct. Mater.* **32**, 2110174 (2022).
43. Yao, Z. et al. Hydrogen radical-boosted electrocatalytic CO_2 reduction using Ni-partnered heteroatomic pairs. *Nat. Commun.* **15**, 9881 (2024).
44. Zhang, L. et al. Elucidating the structure-stability relationship of Cu single-atom catalysts using operando surface-enhanced infrared absorption spectroscopy. *Nat. Commun.* **14**, 8311 (2023).
45. Zhang, X. et al. Molecular engineering of dispersed nickel phthalocyanines on carbon nanotubes for selective CO_2 reduction. *Nat. Energy* **5**, 684–692 (2020).
46. Li, C. Y. et al. In situ probing electrified interfacial water structures at atomically flat surfaces. *Nat. Mater.* **18**, 697–701 (2019).
47. Wang, Y. H. et al. In situ Raman spectroscopy reveals the structure and dissociation of interfacial water. *Nature* **600**, 81–85 (2021).
48. Huang, B. T. et al. Cation-dependent interfacial structures and kinetics for outer-sphere electron-transfer reactions. *J. Phys. Chem. C.* **125**, 4397–4411 (2021).
49. Huang, B. et al. Cation- and pH-dependent hydrogen evolution and oxidation reaction kinetics. *JACS Au* **1**, 1674–1687 (2021).
50. Wang, Y. H. et al. In situ electrochemical Raman spectroscopy and ab initio molecular dynamics study of interfacial water on a single-crystal surface. *Nat. Protoc.* **18**, 883–901 (2023).
51. Zhang, X. et al. Electrochemical oxygen reduction to hydrogen peroxide at practical rates in strong acidic media. *Nat. Commun.* **13**, 2880 (2022).

52. Fan, J. et al. Immobilized tetraalkylammonium cations enable metal-free CO_2 electroreduction in acid and pure water. *Angew. Chem. Int. Ed.* **63**, e202317828 (2024).
53. Kresse, G. & Furthmüller, J. Efficient iterative schemes for ab initio total-energy calculations using a plane-wave basis set. *Phys. Rev. B* **54**, 11169 (1996).
54. Blöchl, P. E. Projector augmented-wave method. *Phys. Rev. B* **50**, 17953 (1994).
55. Perdew, J. P., Burke, K. & Ernzerhof, M. Generalized gradient approximation made simple. *Phys. Rev. Lett.* **77**, 3865 (1996).
56. Grimme, S., Ehrlich, S. & Goerigk, L. Effect of the damping function in dispersion corrected density functional theory. *J. Comput. Chem.* **32**, 1456–1465 (2011).
57. Monkhorst, H. J. & Pack, J. D. Special points for brillouin-zone integrations. *Phys. Rev. B* **13**, 5188 (1976).
58. Cheng, T., Xiao, H. & Goddard, W. A. 3rd Full atomistic reaction mechanism with kinetics for CO reduction on cu (100) from ab initio molecular dynamics free-energy calculations at 298 K. Proc. *Nat. Acad. Sci.* **114**, 1795–1800 (2017).
59. Jarzynski, C. Nonequilibrium equality for free energy differences. *Phys. Rev. Lett.* **78**, 2690 (1997).
60. Zhang, M. D. et al. Continuous electrosynthesis of pure H_2O_2 solution with medical grade concentration by a conductive Ni-phthalocyanine-based covalent organic framework. *J. Am. Chem. Soc.* **146**, 31034–31041 (2024).
61. Ravel, B. & Newville, M. ATHENA, ARTEMIS, HEPHAESTUS: data analysis for X-ray absorption spectroscopy using IFEFFIT. *J. Synchrotron Radiat.* **12**, 537–541 (2005).
62. Zabinsky, S. I. et al. Multiple-scattering calculations of X-ray-absorption spectra. *Phys. Rev. B* **52**, 2995 (1995).

Acknowledgements

The authors thank the following funding agencies for supporting this work: X.Z. acknowledges the Hong Kong Polytechnic University (CD9B, WZ4Q, CDBZ), and the National Natural Science Foundation of China (22205187), Shenzhen Municipal Science and Technology Innovation Commission (JCYJ20230807140402006), and Department of Science and Technology of Guangdong Province (2023A1515110123, 2024A1515012390). K.C. acknowledges the Hong Kong Polytechnic University (CD4L). S.P.L. acknowledges the Hong Kong Polytechnic University (1-CD7U, 1-BBDV). X.L. acknowledges Zhenjiang Key Research and Development Program (GY2021004), and Jiangsu Funding Program for Excellent Postdoctoral Talent (2024ZB736), and the China Postdoctoral Science Foundation (GZC20240614). X.H.Z. acknowledges the Start-up Research Fund of Southeast University and the Big Data Computing Center of Southeast University. The authors acknowledge Shiyanjia Lab (www.shiyanjia.com) for supporting the XPS and TEM analysis.

Author contributions

S.G., Y.Z., and C.J. contributed equally. X.L., X.H.Z., X.Z., and S.P.L. conceived the project and designed the experiments. S.G., X.Z., and S.P.L. conceived the idea. C.J. and Y.Y. performed the theoretical study. S.G., X.H., W.L., Q.X., and J.W. carried out the electrochemical study. X.S., Z.W., and K.C. performed the product gas detection. S.G., X.L., and C.W. performed catalyst characterization. S.G., X.Z., and S.P.L. wrote the manuscript with support from all authors.

Competing interests

The authors declare no competing interests.

Additional information

Supplementary information The online version contains supplementary material available at https://doi.org/10.1038/s41467-025-63722-6.

Correspondence and requests for materials should be addressed to Xiaomeng Lv, Xunhua Zhao, Xiao Zhang or Shu Ping Lau.

Peer review information *Nature Communications* thanks Kai Liu, Jiankang Zhao and the other anonymous reviewer(s) for their contribution to the peer review of this work. A peer review file is available.